

SoilNet: A Multimodal Multitask Model for Hierarchical Classification of Soil Horizons

Teodor Chiaburu^{1*} Vipin Singh^{1*} Frank Haußer^{1†} Felix Bießmann^{1,2†}

¹Berliner Hochschule für Technik ²Einstein Center Digital Future

{chiaburu.teodor,vipin.singh,frank.hausser,felix.biessmann}@bht-berlin.de

Abstract

While recent advances in foundation models have improved the state of the art in many domains, some problems in empirical sciences could not benefit from this progress yet. Soil horizon classification, for instance, remains challenging because of its multimodal and multitask characteristics and a complex hierarchically structured label taxonomy. Accurate classification of soil horizons is crucial for monitoring soil health, which directly impacts agricultural productivity, food security, ecosystem stability and climate resilience. In this work, we propose *SoilNet* - a multimodal multitask model to tackle this problem through a structured modularized pipeline. Our approach integrates image data and geotemporal metadata to first predict depth markers, segmenting the soil profile into horizon candidates. Each segment is characterized by a set of horizon-specific morphological features. Finally, horizon labels are predicted based on the multimodal concatenated feature vector, leveraging a graph-based label representation to account for the complex hierarchical relationships among soil horizons. Our method is designed to address complex hierarchical classification, where the number of possible labels is very large, imbalanced and non-trivially structured. We demonstrate the effectiveness of our approach on a real-world soil profile dataset. All code and experiments can be found in our repository: <https://github.com/calgo-lab/BGR/>.

1 Introduction

Soils are essential to life on Earth, serving as the foundation for ecosystems, agriculture and water filtration. They support plant growth, regulate the carbon cycle and influence biodiversity, making soil health a direct determinant of food security, environmental resilience and public well-being. Assessing soil quality is, therefore, critical, as it reflects both natural conditions and human impact. However, modern pressures such as pollution, deforestation and climate change are accelerating soil degradation. Industrial contaminants, excessive pesticide use and shifts in climate patterns can disrupt soil composition, reduce fertility and increase erosion and desertification [1]. These challenges highlight the urgent need for scalable reliable methods to monitor and analyze soil quality.

A key aspect of soil quality assessment is the characterization of its vertical and lateral structure, which consists of distinct layers known as *soil horizons* [17]. In pedology, these horizons are classified based on their physical, chemical and biological properties, providing essential insights into soil formation processes (*pedogenesis* [35]) and fertility. Accurately identifying and classifying soil horizons is important for applications ranging from agriculture to environmental monitoring and land management. However, this task is inherently complex, given the highly variable nature of soil profiles across different regions and the intricate dependencies between horizon types. As illustrated

*Equal contribution.

†Equal supervision.

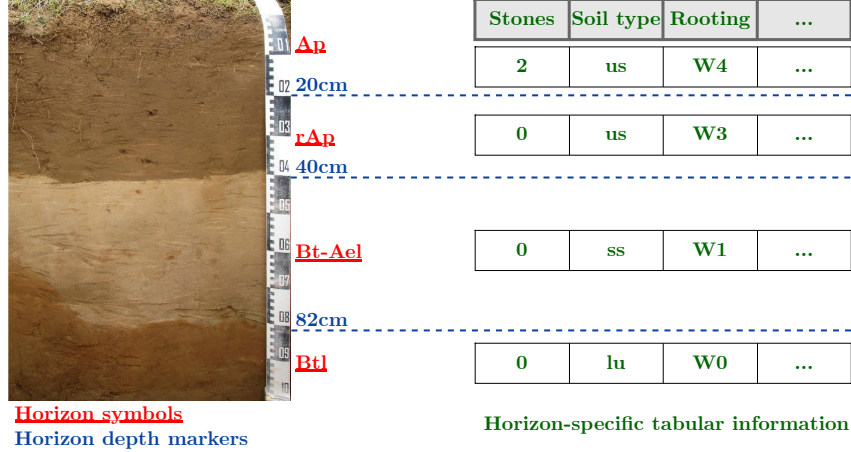


Figure 1: Example of an annotated soil profile. The ruler on the right margin marks the 1-meter depth of the photographic probe. The soil profile has 4 horizons, with annotated labels (in red), segment borders (in blue) and morphological properties (in green). Soil images and data provided by: [42, 7].

in Figure 1, such expert annotations are highly specialized and cannot be effectively performed using generic prompting approaches with large language models (LLMs) - see Appendix A.

Traditional soil classification follows a hierarchical taxonomy [21], but in practice, soil horizons exhibit overlapping characteristics and multiple parent-child relationships, making them better represented as a graph-structured taxonomy rather than a simple tree. A single horizon can share properties with multiple others and transitional layers further complicate the classification process. This complexity, combined with the class imbalance in real-world soil datasets, makes automated horizon classification particularly challenging.

To address these challenges, we introduce *SoilNet*, a novel multimodal framework for automated soil horizon description. Our approach sequentially predicts depth markers based on image data and geotemporal metadata e.g. geographical location, month, relief type, effectively segmenting soil profiles into meaningful horizon intervals. Each segmented region is then described by a set of physical/morphological soil features e.g. color, humus content or rooting pattern. A key aspect of our method is the use of graph-based embeddings to represent the horizon labels, capturing their complex interdependencies beyond a rigid hierarchical taxonomy.

The main contributions of our work are as follows:

1. We formulate the soil horizon classification task as a structured, multimodal, multitask problem, decomposed into a three-stage pipeline that mirrors the expert decision-making process in pedology:
 - (a) **Task 1 – Segmentation:** We predict a variable-length sequence of *depth markers* that segment the soil profile image into sequential horizon candidates.
 - (b) **Task 2 – Morphological Feature Prediction:** For each predicted segment, we estimate a set of *tabular morphological properties* (e.g., soil color, humus content), serving as a reproduction of the horizons’ metadata.
 - (c) **Task 3 – Horizon Classification:** Finally, we classify each horizon segment using *hierarchical label embeddings*, accounting for the complex taxonomy of soil horizons.
2. We introduce **SoilNet**, a novel end-to-end training and inference framework that integrates image and tabular modalities, sequential segmentation, intermediate tabular predictors and graph-based label reasoning. The model is modular by design, enabling transparent evaluation of each stage and facilitating adaptation to similar hierarchical segmentation and classification tasks in other domains.

2 Related Work

Automatic Soil Classification. Developing automated Machine Learning (ML) methods for classifying soil horizons and types or predicting various soil properties has been an active field of research throughout the past years. The study in [5] evaluates CNNs for classifying acid sulfate soils. The research in [31] combines soil spectral reflectance with standard ML methods like SVMs or Random Forests. [33, 16] train CNNs to classify soil types based on their ground surface color. An in-depth review of the current ML strategies used for soil classification can be found in [14, 32, 41].

Sequential Segmentation. Modeling sequential outputs, where the prediction at each step depends on previous outputs and contextual cues is highly relevant to our task of sequentially segmenting soil profile images from top to bottom into horizon boundaries. A widely adopted solution in such settings is the use of Long Short-Term Memory (LSTM) networks [34]. More recently, *Cross Attention* mechanisms within Transformer architectures have emerged as a powerful alternative for sequence modeling [9, 11, 19, 27]. In a similar geological use-case, [44] applies various Deep Learning techniques to segment fine roots from time series images of soil profiles, in order to investigate the dynamics of fine roots areas over time, while [23] apply semantic segmentation to directly localize and classify soil horizons into main symbols A, B, C. In a different application scenario (medicine), but with comparable sequential structure, the authors in [37] segment retinal layers in tomographic images with CNN-based models by predicting the contours of their boundaries.

Hierarchical Classification. Hierarchical structures are a common characteristic across a wide range of ML tasks. In computer vision, efforts to incorporate class hierarchies into image classifiers typically fall into three categories [4]. The first includes *label/graph embedding* approaches [3, 30], which represent labels as vectors in a continuous space to capture semantic relationships (typically derived from a tree or graph). The second group focuses on *hierarchy-aware loss functions* [4, 10], which encourage predictions that are consistent with the underlying class taxonomy. The third category involves *hierarchical architectures* [46, 45] that integrate the hierarchical structure directly into the network design. Recent advancements explore hierarchical segmentation [26], combining the aforementioned strategies to directly enforce the label hierarchy on the segmentation task.

Multimodal/Multitask Models. Recent work in natural language processing has led to the development of large language models (LLMs) that serve as general-purpose multitask solvers, capable of addressing a wide range of linguistic tasks in both zero-shot and few-shot scenarios [6]. Efforts to extend these models into multimodal domains have followed three main directions. One line of work focuses on unifying vision and language inputs within a single architecture to enable perception and reasoning across different modalities [2, 22]. Another direction explores the integration of external tools and models into LLM pipelines, allowing them to dynamically invoke specialized modules such as visual encoders or programmatic solvers [40, 13]. A third direction treats the LLM as a centralized controller responsible for orchestrating a collection of expert models across modalities [38, 28]. Rather than solving tasks directly, the LLM interprets user intent, selects appropriate external models based on their capabilities and manages inter-model communication.

We note that, to the best of our knowledge, none of the current ML approaches leverages multimodal input for classifying soil horizons (the typical input is images). In contrast, our work combines visual input with tabular metadata. This offers a much richer signal to the classifier. A more in-depth discussion is provided in subsection 4.2.

3 Data

For carrying out the experiments and training our models we disposed of an image-tabular dataset built and curated by our partner geological institutes [7] and [42]. This dataset is, to the best of our knowledge, the most comprehensive multimodal dataset in the automatic soil classification literature. A detailed overview of other datasets used for developing automatic soil classifiers can be found in [15]. In the following, we describe the data and the preprocessing methods. For the time being, the full dataset cannot be made publicly available. For a detailed description of the data acquisition and annotation procedures we refer the reader to [21].

The visual modality in our dataset consists of **3349 soil profile images** collected by geologists during fieldwork. A rectangular pit approximately 1 meter deep was excavated at each sampling location to expose a vertical cross-section of the soil. Researchers then captured frontal images of the exposed soil wall, where natural stratification into horizons is visible through color, texture and structural variation (see example in Figure 1). These photographs provide a consistent top-down view of the soil profile, with the surface typically aligned at the top of the frame and the bottom corresponding to a depth of around -1 meter. From the original profile images we have removed the ruler with SAM [25] and, whenever necessary, the sky background visible above the ground with a standard thresholding algorithm. This way, the resulting images correspond from top to bottom to the 1-meter-range of the sample.

The profile images are accompanied by a set of additional annotations, stored in **tabular form**. These include some that are horizon-specific and others that describe the whole sample, such as associated geotemporal data. In total, the dataset contains metadata for **13621 horizons** and **1218 horizon classes** (clustered as 99 classes, see subsection 4.3). We emphasize that different soil samples may exhibit a different number of horizons (every sample in the dataset has at least 2 horizons and at most 8). A detailed description of the tabular data is given below.

Below we describe the tabular data in detail:

Geotemporal Information. For each soil sample, the geographical location (as latitude/longitude coordinates) and the date (month and year) were recorded. Further information (derivable from time and position) was stored as well e.g. type of relief form, soil climate zone, peat thickness, soil curvature, groundwater level and so on. These properties describe the excavation spot as a whole and are not horizon specific.

Depth Markers. The borders between the soil horizons are described by vertical markers stored as integers from 0 cm (ground level) to 100 cm (the deepest level of the excavated sample) - Figure 1. Please note that the depth markers are approximations of the true boundaries between the horizons, which are often non-linear and irregular.

Morphological (Horizon-Specific) Information. After segmenting the soil into horizons and upon further scrutiny and tests, the geologists annotate each horizon with an additional set of morphological/physical characteristics. There are 6 such features in our dataset:

- *Number of stones* [numerical]: To roughly estimate the gravel presence, geologists manually counted the small stones within each soil horizon. Their numbers range from 0 to 100 in our dataset.
- *Soil type* [categorical]: The classification of soil type is based on the relative proportions of three fine soil fractions: *sand*, *silt* and *clay*. Depending on which fraction dominates, soils are roughly categorized as sandy, silty or clayey; after taking further finer-grained features into consideration e.g. granularity or compactness, the three main classes are split into subclasses. To reduce sparsity, in collaboration with our domain experts we have clustered the 58 soil types in our dataset down to 17 classes.
- *Soil color* [categorical]: Field geologists annotate soil color³ using the standardized **Munsell color system**, which specifies color through three components: *hue*, *value* (lightness) and *chroma* (intensity). For example, a typical soil color might be recorded as *10YR 5/3*, indicating a yellowish-brown hue with medium lightness and moderate saturation. To reduce the complexity and sparsity of the color label space, we discretized the value and chroma axes into 2-by-2 grids, grouping them into coarser intervals. By doing this, we arrived at 74 color classes from 254.
- *Carbonate content* [categorical]: Carbonate content refers to the presence of calcium carbonate (CaCO_3) and calcium-magnesium carbonate ($\text{CaMg}(\text{CO}_3)_2$). In our dataset, this property is discretized into levels ranging from *C0* (no detectable carbonate) to *C6* (very high carbonate concentration).

³We note that other authors e.g. [16] refer to the ground surface color as the 'soil color'. In our work, soil color is horizon specific and denotes the color of a specific horizon stripe below the ground level.

- *Humus content* [categorical]: Humus content reflects the amount of decomposed organic matter present in a soil horizon. Humus forms through the microbial breakdown of plant and animal residues and plays a key role in soil fertility and structure. Our dataset categorizes this property using a discrete scale from *h0* (no visible humus) to *h7* (very high humus concentration).
- *Rooting* [categorical]: Rooting is measured as the average number of roots per dm^2 and is categorized on a discrete scale from *W0* (no roots) to *W6* (high number of roots).

Horizon Labels. The most central component of the tabular data is the soil horizon labels, which encode expert geological interpretation of the morphological and compositional characteristics of each soil layer. These labels follow a domain-specific label grammar standardized in German pedology, where each symbol consists of a mandatory uppercase main symbol e.g. **A**, **B**, **C**, that denotes the principal genetic horizon, optionally preceded and/or followed by lowercase modifiers. Prefix letters, appearing before the main symbol e.g. **rA**, **ilC**, indicate geogenic or anthropogenic influences, such as stratification or human disturbance. Suffix letters, following the main symbol e.g. **Bv**, **Ah**, describe pedogenic features such as accumulation of clay, organic matter enrichment or carbonate presence. While these components can, in theory, be combined, not all combinations are valid; certain modifiers are restricted to specific main horizon types due to their geological interpretation. For example, the prefix **a** cannot appear before **B** to form **aB**. While other countries follow different taxonomic systems adapted to the pedologic reality of their regions [39], it is an international convention in pedology to encode horizon properties with structured combinations of upper- and lowercase letters.

In addition to singular horizon labels, the dataset also contains **mixture symbols**, which denote transition zones between two adjacent horizons that exhibit characteristics of both. These occur along visually or chemically gradual boundaries and are represented by combining two valid horizon symbols with an operator, such as '+', '-', or 'o', each reflecting a different type of transition. For simplification, we normalize all such mixtures using the '-' operator e.g. **Ah-Bv**, regardless of the original transition type.

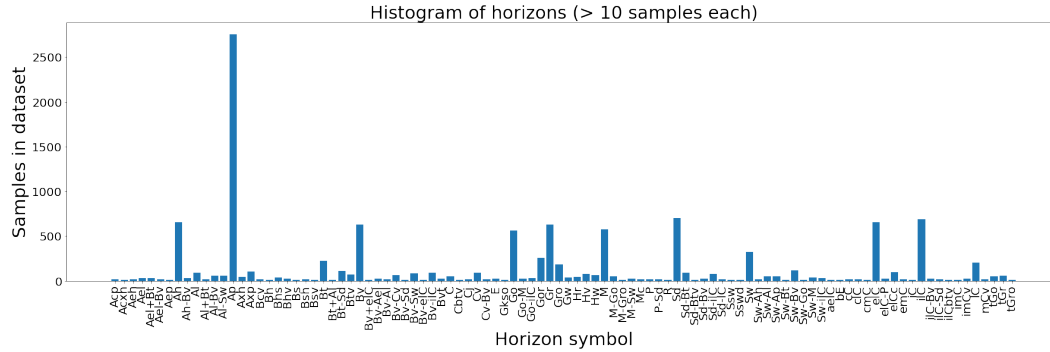


Figure 2: Distribution of horizon symbols with more than 10 samples in the whole dataset (out of 13621 horizon samples in total). For training, we combine both mixture operators '-' and '+' into one single general mixture operator '-'.

With this aggregation considered, there are 1218 different horizon symbols in our dataset, spread over a highly skewed distribution. Upon consulting with our domain experts, they constructed a mapping to simplify the labels into shorter and more concise strings. From these simplified labels, we kept those that have more than 10 samples in the dataset as such; this resulted in **99 final horizon symbols** - see Figure 2 for their distribution. The remaining less frequent ones were clustered onto the most (geologically) relevant symbol from the 99 ones. For details regarding this label clustering process, please consult subsection 4.3.

The remaining 99 symbols are underlain by a directed acyclic graph, visualized completely in Figure 3. One particularity about the horizon symbol graph is that terminal nodes corresponding to the mixture symbols e.g. **Al-Bt** spawn from two parent nodes, one for each individual mixture member. It is this property that differentiates our taxonomic graph from a tree.

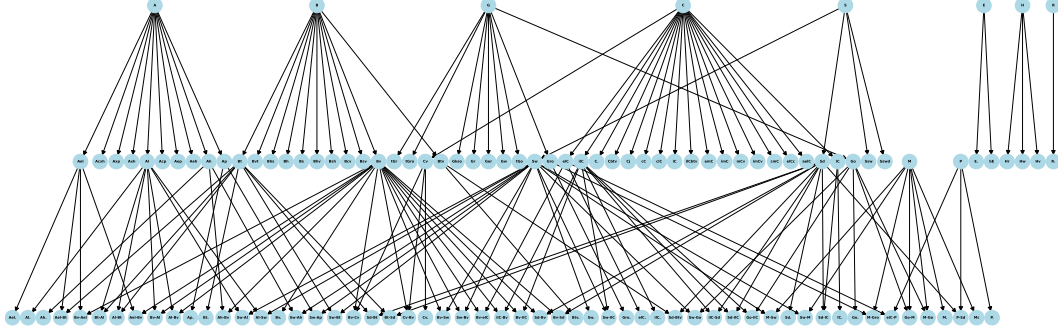


Figure 3: Graph taxonomy of the horizon labels with more than 10 samples each. The abstract Root node, from which the main symbols branch out, is not drawn here for better readability. All leaf nodes represent the labels present in the training set. Please note that the lowest level of the graph also contains mixture nodes that derive properties from two parent nodes. Therefore, the hierarchical graph is not a tree.

Data Split. For training our models we split the dataset into training/validation/test subsets in a proportion of 60-20-20%. To maintain the distribution of the horizon symbols and the categorical tabular horizon features used in solving Task 3 and Task 2 (see subsection 4.1), respectively, we applied a Multilabel Stratified Split [36]. For more details regarding the preprocessing of the dataset in preparation for the training process please consult our code repository.

4 Methods

In this section we describe the overall workflow of our proposed approach followed by a more in-depth description of the key components in the SoilNet architecture.

4.1 Formulation of the Tasks

To match the experts’ approach when classifying soil horizons, we break down the general classification problem into three tasks, meant to fully describe the horizons (see Figure 4).

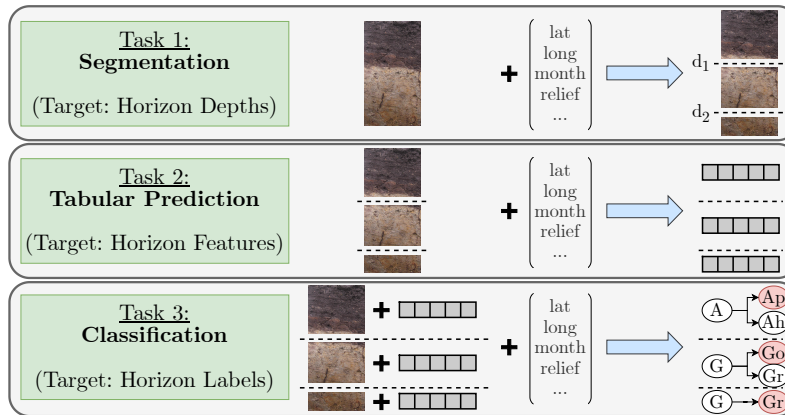


Figure 4: Task 1: Soil profile images are segmented based on features extracted from the full images concatenated with features extracted from the geotemporal data. **Task 2:** Tabular morphological features are predicted based on (visual) features extracted from the segments concatenated with the geotemporal features (one set of tabular features per segment). **Task 3:** Horizon labels are predicted based on concatenated visual segment features, geotemporal features and tabular morphological features (one label per segment). Soil images and data provided by: [42, 7].

4.2 SoilNet

The inner mechanisms of SoilNet are depicted in Figure 5. Our model processes images as the one shown in Figure 1 and geotemporal metadata to sequentially predict depth markers, extract morphological (tabular) properties and classify soil horizons using a graph-based embedding approach. Our ablation studies in section 5 compare this to a straightforward cross-entropy loss. Below, we describe each key component of SoilNet in short. For more technical details regarding the implementation of the modules and the models, please consult our repository.

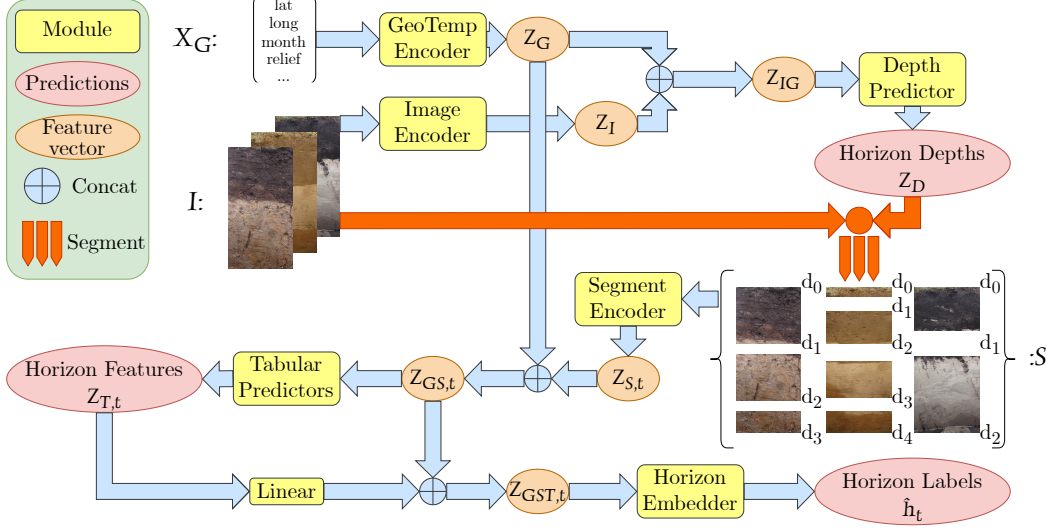


Figure 5: An illustration of our proposed modularized multimodal multitask architecture for solving the three tasks (**SoilNet**). Soil images and data provided by: [42, 7].

Image Encoder. The image encoder extracts visual features from the soil profile images. Given an input RGB-image I , SoilNet applies a convolutional neural network (CNN) to extract visual features:

$$\mathbf{z}_I = f_{\text{img}}(I) \in \mathbb{R}^{d_I} \quad (1)$$

where f_{img} represents the CNN-based feature extractor and d_I is the dimensionality of the extracted feature vector. The soil profile images in the data exhibit significant variations in shape and resolution. Batch-processing requires all images to have the same dimensions. However, resizing the images to a dimension too low would lead to a distortion in the profile geometry and significant blurring of the very fine horizon features. We avoided this by padding the images to equal sizes. In the image encoder, we used a ResNet18 backbone [18] (initialized with ImageNet weights). Instead of standard average pooling, we compute a masked average pooling to only consider features corresponding to the unpadded image. The output is afterwards linearly projected onto the d_I -dimensional latent space. We denote this module as Masked ResNet.

Geotemporal Encoder. Geospatial and temporal information plays an important role in determining soil characteristics. Geotemporal features are represented as a vector

$$\mathbf{x}_G = [\text{lat}, \text{long}, \mathbb{1}(\text{month}), \mathbb{1}(\text{year}), \mathbb{1}(\text{relief type}), \dots] \in \mathbb{R}^G \quad (2)$$

where lat , long correspond to geographic coordinates and $\mathbb{1}(\cdot)$ are one-hot encodings of the categorical features. With acquiring this kind of data, the idea is that auxiliary relief and climate characteristics can be derived from the location and timestamp stored when taking the photo of the soil sample (for instance, on the annotator’s photo camera). The vector x_G containing the geotemporal data is then processed by f_{geo} - a fully connected neural network (MLP)

$$\mathbf{z}_G = f_{\text{geo}}(\mathbf{x}_G) \in \mathbb{R}^{d_G} \quad (3)$$

producing an encoded representation of geotemporal properties.

Depth Predictor. To segment the soil profile into horizons, we sequentially predict depth markers. Given the concatenated feature representation

$$\mathbf{z}_{IG} = [\mathbf{z}_I; \mathbf{z}_G] \in \mathbb{R}^{d_I+d_G} \quad (4)$$

where $[\cdot; \cdot]$ denotes concatenation along the feature axis, we use an LSTM module [34] preceded and succeeded by a Linear layer to generate a sequence of depth markers:

$$\mathbf{z}_D = [d_1, d_2, \dots, d_D], \quad d_t = f_{\text{depth}}(\mathbf{h}_{t-1}, \mathbf{z}_{IG}), \quad \forall t = 1, \dots, D \quad (5)$$

where f_{depth} is the LSTM-based depth predictor, \mathbf{h}_{t-1} is the hidden state at step $t-1$ and D is the number of predicted horizons. Every $d_t \in (0, 1]$ is a proposal for the lower boundary of the horizon at step t . Depth markers in the dataset, originally given in centimeters (0-100), were converted to meters. For example, $d_1 = 0.3$ indicates that the topmost horizon ends at -0.3 meters. We emphasize that soil samples can have a different number of horizons, so the vector \mathbf{z}_D may have variable lengths for different inputs \mathbf{z}_{IG} . We decided to pad the output \mathbf{z}_D , so that D is a fixed maximal sequence length for every sample. Concretely, once d_t is within a margin of $\epsilon = 0.01$ meters to the value of a *stop token* s (here, 1 meter depth), the marker is rounded to s .

Segment Encoder. Once depth markers are predicted, they are used to crop the original profile images down to the proposed horizon segments. Each segment $[d_{t-1}, d_t]$ defines a horizontal stripe of the image (see Figure 1), which is processed by a second CNN-based encoder:

$$\mathbf{z}_{S,t} = f_{\text{seg}}(I_{[d_{t-1}, d_t]}) \in \mathbb{R}^{d_S} \quad (6)$$

where f_{seg} represents the CNN backbone and $I_{[d_{t-1}, d_t]}$ is the cropped image region corresponding to the predicted soil horizon. For $t = 1$, d_0 is set to 0, representing the zero marker on the soil surface. Similar to the image encoder, we need to handle segments of variable sizes. We experimented with two patch-based strategies for f_{seg} :

1. **Grid-based Patching (PatchCNN):** Segments are resized to 512×1024 pixels (a higher resolution than the standard 224-pixel requirement of standard visual CNNs). A 1×2 symmetrical grid is applied to extract patches of a fixed size 512×512 , which are then processed by a custom 5-layer CNN.
2. **Random Patching with ResNet:** From the segments cropped out of the original images, we randomly extract 48 patches of size 224×224 . The patches are then processed by a standard ResNet18 backbone.

Both approaches average the feature vectors for all patches into one single feature vector for each segment. In section 5, we compare the performance of the two approaches.

Tabular Predictors. At this stage, SoilNet predicts the morphological tabular features for each segmented region. For a given segment $[d_{t-1}, d_t]$, the following vector is formed:

$$\mathbf{z}_{GS,t} = [\mathbf{z}_G; \mathbf{z}_{S,t}] \in \mathbb{R}^{d_G+d_S} \quad (7)$$

This concatenated vector is processed by a set of tabular predictors of a similar LSTM-based architecture as the depth predictor's. The output is the set of tabular properties:

$$\mathbf{z}_{T,t}^i = f_{\text{tab}}^i(\mathbf{z}_{GS,t}) \in \mathbb{R}^{m_i}, \quad \forall i = 1, \dots, M \quad (8)$$

where M is the number of morphological attributes e.g. soil color, humus class. The dimension m_i of the i -th tabular feature vector is 1 for numerical features (like the number of stones) or the number of unique classes for categorical features (such as the humus content). f_{tab}^i is, hence, the module responsible for predicting the i -th tabular feature in the form $\mathbf{z}_{T,t}^i$ for the horizon at step t . We denote by $\mathbf{z}_{T,t}$ the concatenation of all the outputs of the tabular predictors:

$$\mathbf{z}_{T,t} = [\mathbf{z}_{T,t}^1; \dots; \mathbf{z}_{T,t}^M] \in \mathbb{R}^m \quad (9)$$

where $m = \sum_i^M m_i$.

Horizon Embedder. Finally, soil horizons are classified using a graph-based embedding approach, which we extended from the algorithm in [3]. Each possible target horizon label h_i (given as string or class index) is represented by an embedding vector

$$\varphi(h_i) \in \mathbb{R}^{d_E}, \forall i = 1, \dots, N \quad (10)$$

computed from a graph of horizon relationships, where edges represent hierarchical and compositional dependencies (see Figure 3). Note that $N \geq d_E$ since the embeddings of mixture labels are linear combinations of independent non-mixture embeddings. The horizon embedder f_{hor} takes as input the final concatenated vector

$$\mathbf{z}_{GST,t} = [\mathbf{z}_{GS,t}; \text{Lin}(\mathbf{z}_{T,t})] \in \mathbb{R}^{d_G+d_S+m_{\text{in}}} \quad (11)$$

where $\text{Lin}(\mathbf{z}_{T,t}) \in \mathbb{R}^{m_{\text{in}}}$ is the linear projection of the tabular predictions $\mathbf{z}_{T,t}$ and

$$\hat{\mathbf{y}}_t = f_{\text{hor}}(\mathbf{z}_{GST,t}) \in \mathbb{R}^{d_E} \quad (12)$$

delivers the embedding prediction $\hat{\mathbf{y}}_t$ for the horizon candidate at step t . The predicted horizon class \hat{h}_t is inferred via a similarity score $s(\hat{\mathbf{y}}_t, \varphi(h_i))$ (for instance, cosine similarity) as

$$\hat{h}_t = \arg \max_i s(\hat{\mathbf{y}}_t, \varphi(h_i)). \quad (13)$$

subsection 4.4 explains in detail how we computed the horizon embeddings and Appendix B gives a numerical calculation example.

When training the whole SoilNet pipeline end-to-end, we optimized a weighted sum of all the individual losses:

$$L_{\text{total}} = 10L_{\text{depth}} + \frac{1}{10}L_{\text{stones}} + \sum_i^{M_{\text{categ}}} L_{\text{categ}_i} + 10L_{\text{horizon}} \quad (14)$$

where $M_{\text{categ}} = 5$ is the number of categorical morphological properties (soil type, color, humus class, rooting and carbonate). The weights were derived from the individual loss scales when training the task solvers separately.

4.3 Label Clustering

The horizon classification problem (Task 3) is highly imbalanced, with some horizon labels being well-represented while others appear very rarely in the dataset (see Figure 2). Directly training a model on such an imbalanced label set leads to poor generalization for rare horizons and biased predictions towards the over-represented classes. To mitigate this, we employ a clustering approach that groups similar horizons while preserving the structure of the taxonomic hierarchy.

First, we filter the set of horizon labels by retaining only those with more than 10 samples in the dataset. Let H be the full set of horizon labels. We define the filtered set of representative labels as $V = \{h_1, h_2, \dots, h_N\} \subset H$ (which will also be the set of terminal nodes in the taxonomic graph described in Figure 3 and subsection 4.4). These selected labels form the classification targets for Task 3.

Rare horizon labels $h_r \in H \setminus V$ with a maximum of 10 samples in the dataset are assigned to the closest label in V using a string similarity measure. Specifically, we use the *Levenshtein distance* $d_L(h_r, h)$, which quantifies the number of character edits (insertions, deletions, substitutions) needed to transform one label into another [43]. The assignment is performed as

$$h_r \mapsto \arg \min_{h \in V} d_L(h_r, h) \quad (15)$$

After applying the Levenshtein mappings, we needed to carry out a final rule-based correction step, since some of the mappings were not geologically plausible. We implemented these rules after consulting our domain experts.

4.4 Graph Embeddings

Soil horizons exhibit complex relationships that cannot be adequately captured by a simple tree-based taxonomy. Instead, they form a *graph-structured taxonomy*, where certain horizons have

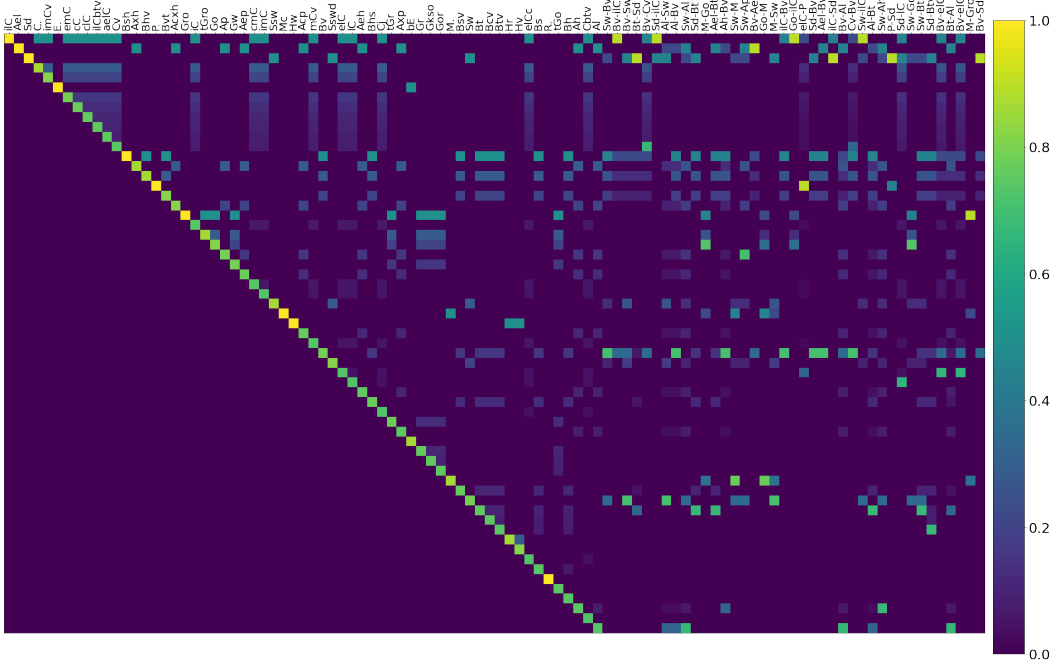


Figure 6: Heatmap visualizing the horizon embeddings. The matrix has dimension $(d_E \times N) = (61 \times 99)$. The left 61×61 block is diagonal and contains the embeddings of the non-mixture labels. The right 61×38 block contains the embeddings of the mixture labels.

multiple parent nodes due to transitional characteristics and mixtures (see Figure 3). To incorporate this structure into the model, we construct *hierarchical embeddings* according to the method described in [3] and introduce an additional step to compute representations for mixture horizons.

Let the set of soil horizon labels be represented as a directed acyclic graph $G = (V, \varepsilon)$, where V is the set of all horizon classes and $\varepsilon \subset V \times V$ defines parent-child relationships⁴. Furthermore, let V^- be the subset of non-mixture horizon labels and V^+ the complement with mixture labels, so $V^- \cup V^+ = V$ and $V^- \cap V^+ = \emptyset$. The semantic similarity between two horizon labels $h_i, h_j \in V^-$ is computed based on the height of their lowest common ancestor (LCA) in the hierarchy:

$$d_G(h_i, h_j) = \frac{\text{height}(\text{LCA}(h_i, h_j))}{\max_{h \in V^-} \text{height}(h)} \quad (16)$$

which is then converted into a similarity score:

$$s_G(h_i, h_j) = 1 - d_G(h_i, h_j). \quad (17)$$

Following [3], each non-mixture horizon label h_i is embedded into a vector space such that their dot products reflect these similarity scores:

$$\varphi(h_i)^\top \varphi(h_j) = s_G(h_i, h_j). \quad (18)$$

To ensure all embeddings lie on a unit hypersphere, they are normalized as

$$\|\varphi(h_i)\|_2 = 1. \quad (19)$$

Embeddings are computed iteratively, starting from an abstract root node and adding new nodes while maintaining the required pairwise similarities. Please refer to Appendix B for an example of computing several embeddings this way.

Mixture horizons, which inherit properties from not one, but two parent nodes, are represented as a linear combination of the embeddings of both their parents, emphasizing the second symbol more:

$$\varphi(h_{\text{mix}}) = \frac{1}{3}\varphi(h_{\text{parent}_1}) + \frac{2}{3}\varphi(h_{\text{parent}_2}) \quad \forall h_{\text{mix}} \in V^+ \quad (20)$$

⁴We use here the notation ε to denote the edges referred to as E in [3], to avoid confusion with the symbol E in d_E we already introduced in subsection 4.2.

This ensures that mixture horizons are positioned meaningfully within the embedding space, preserving their semantic relationships to both parent horizons. Instead of fixing the weights, one could learn them as hyperparameters. Upon consulting with our geological experts, who are generally more interested in the correct classification of the second label of a mixture (marked as dominant also in [21]), we concluded that weighting $\varphi(h_{\text{parent}_2})$ twice as much as $\varphi(h_{\text{parent}_1})$ serves our purposes well enough. Figure 6 displays the $d_E \times N$ embedding matrix as a color map. The first $d_E \times d_E$ block contains the independent non-mixture embeddings, while the remaining $d_E \times (N - d_E)$ block lists the mixture embeddings.

4.5 Teacher Forcing

We also investigate the impact of different teacher forcing strategies during training, inspired by similar standard approaches from sequence-to-sequence modeling [29]. We have implemented teacher forcing within SoilNet at the steps where the inputs for learning Task 2 and 3 are prepared.

We experiment with two teacher forcing paradigms:

1. **Full teacher forcing:** The model is trained with the ground-truth depth markers and tabular horizon features as inputs for all training samples. This means that the model is not exposed to any of its own predictions during training.
2. **Linearly decreasing teacher forcing:** The model is trained with the ground-truth depth markers and tabular horizon features as inputs for the first five epochs. With each progressing epoch of these five, the teacher-forcing rate decreases, until the model is trained solely with its own predictions as inputs.

5 Results

This section presents the main results of our experiments and is divided into two subsections: **Individual Tasks** and **End-to-End Pipeline**. The Individual Tasks denote the three tasks shown in Figure 4 solved disjointly (one separate model for each task), while the End-to-End Pipeline refers to the three tasks approached in a joint training and evaluation setting, as depicted in the SoilNet architecture in Figure 5. We report established metrics such as Mean Squared Error (MSE) for regression, Precision/Recall@k for classification tasks and a one-dimensional Intersection-over-Union (IoU) for the segmentation task. To account for the hierarchical nature of the label space we also compute an aggregated accuracy that reflects deviations from the primary horizon symbol, as detailed in Appendix C. The hyperparameters and compute resources are also provided in Appendix C.

5.1 Individual Tasks

In the Individual Tasks stage, we train disconnected task solvers for the three proposed tasks. Concretely, the Individual Depth Predictor only solves Task 1 using full images and geotemporal features as input. The Individual Tabular Predictor only solves Task 2 using visual features from the horizon stripes (segmented with the ground truth depth markers) and geotemporal features. Finally, the Individual Horizon Predictor only solves Task 3 using features combined from the true horizon segments, geotemporal data and the true horizon tabular data. The insights gained from training the task solvers separately were subsequently used to construct the end-to-end SoilNet architecture. Additionally, the performance of the individual task solvers is meant to estimate an upper bound for the end-to-end solver (SoilNet). In the following, we will shortly discuss these insights and present the evaluating metrics for the different configurations. The best individual task solvers trained with the ground truth data will also be displayed in Table 4.

Task 1: Individual Depth Prediction. We first compared the performance of two depth predictor configurations, which differ in the depth prediction module itself: one LSTM-based, one Cross-Attention-based. In both cases, the visual features are extracted via the Masked ResNet Image Encoder described in subsection 4.2. The best Task 1 solver achieves an IoU of 51.74%. For

comparison, an average 'random chance' depth predictor⁵ achieves an IoU of 44.06%. Table 1 shows the metrics for the two configurations of the individual depth predictor.

Table 1: LSTM-based depth predictor outperforms Cross-Attention module. The 1D-IoU scores are computed on the test set and given in percents (%).

DP = Depth Predictor, MaskedResNet = image encoder and {LSTM, CrossAtt} = depth predicting module.

Model name	IoU (%)
Average prediction	44.06
DP_MaskedResNet_LSTM	51.74
DP_MaskedResNet_CrossAtt	50.40

Task 2: Individual Tabular Prediction. Secondly, we trained two configurations of Task 2 solvers by swapping the visual encoders for the true horizon segments: the custom PatchCNN and the ResNet-based one, see *Segment Encoder* in subsection 4.2. A ResNet-based segment encoder outperforms the custom PatchCNN encoder. The best Task 2 solver achieves an average accuracy of 47.59% for the categorical features and a mean squared error (MSE) of 1.30 for the numerical feature (the number of stones). Table 2 shows the metrics for the two configurations of the individual tabular predictor. Both configurations use LSTM as tabular prediction modules for the six tabular horizon features. For better readability, we show the aggregated metrics for the categorical features in Table 2. The full metrics tables for the individual horizon-specific tabular predictions are shown in Appendix D, see Table 6.

Table 2: ResNet-based tabular predictor outperforms the custom PatchCNN-based tabular predictor. All metrics are computed on the test set and given in percents (%), except MSE. The classification metrics are averaged over the six categorical features. See Table 6 for the full table.

TP = Tabular Predictor, {PatchCNN, ResNet} = segment encoder, LSTM = tabular prediction module, Acc. = Accuracy, Prec. = Precision, Rec. = Recall.

Model name	Stones	Categorical Features (Mean) - Metrics in %						
	MSE	Acc.	F1	Prec.	Rec.	Acc.@3	Prec.@3	Rec.@3
TP_PatchCNN_LSTM	6.11	44.53	20.22	27.47	21.39	74.67	61.68	47.52
TP_ResNet_LSTM	1.30	47.59	24.15	29.44	25.52	77.92	68.01	54.14

Task 3: Individual Horizon Prediction. Thirdly, we trained Task 3 solvers under the assumption that both the ground truth depth markers and the ground truth horizon-specific tabular features are provided as input. We evaluated four configurations: two visual segment encoders (PatchCNN vs ResNet-based) and two loss functions (cosine embedding loss - as described in *Horizon Embedder* in subsection 4.2 - vs cross-entropy loss). The main results are presented in Table 3. The results highlight the difficulty of Task 3, particularly in recognizing horizons from the long tail of the label distribution (very low F1 scores). On the other hand, the top-5 metrics indicate that the correct horizon label is frequently among the model's top-ranked predictions. Similarly, the aggregated main symbol accuracies reveal that models are often able to correctly identify the primary symbol of a horizon. This effect is especially pronounced in configurations trained with cosine embedding loss, suggesting that the learned label embeddings effectively model both intra-class similarity and inter-class variability, leading to more geologically coherent predictions (see Appendix E, where we present corresponding confusion matrices).

⁵The average depth predictor simply responds with the average ground truth vector of depth markers computed on our training set.

Table 3: Graph embeddings lead to a higher aggregated accuracy over the main symbol than traditional one-hot encodings. All metrics are computed on the test set and given in percents (%). HP = Horizon Predictor, {PatchCNN, ResNet} = segment encoder, LSTM = horizon embedding/classification module, Emb = embedding loss, CE = cross entropy, Acc. = Accuracy, Prec. = Precision, Rec. = Recall, Agg. Acc. = Aggregated Accuracy over main symbols.

Model name	Acc.	F1	Acc.@5	Prec.@5	Rec.@5	Agg. Acc.
HP_PatchCNN_LSTM_Emb	47.62	14.23	71.68	55.04	47.21	78.99
HP_ResNet_LSTM_Emb	47.75	14.69	72.27	50.56	49.01	78.99
HP_PatchCNN_LSTM_CE	51.55	10.07	78.89	56.38	37.55	73.84
HP_ResNet_LSTM_CE	48.14	11.13	78.88	59.00	44.03	69.41

5.2 End-to-end Pipeline: SoilNet

With what we have learned from training the individual task solvers above, we have designed the SoilNet architecture - an end-to-end pipeline capable of solving all three tasks simultaneously - as shown in Figure 5.

Table 4 compares the results for various configurations of the SoilNet model (partitions C and D) with baseline models (partitions A and B) and the individual task solvers’ results (partition E). Table 4 (partition A) reports the zero-shot performance of a LLM for simplified versions of Tasks 1 and 3; for details on the LLM inference we refer to Appendix A. The baseline models in Table 4 (partition B) are chained individual task solvers. Here, each solver consumes the outputs of the respective previous task solver. In partition E, we report the best performing module configuration for individual task solvers with access to the ground truth of the respective previous task (for a more detailed overview, consult the previous subsection 5.1). Note that since ground truth from previous tasks is not available in real world applications, we do not include these in the model comparison. Results in partitions B and E can be considered lower bounds (using naive chaining of Task solvers’ outputs) and upper bounds (with access to ground truth of previous tasks) for each task.

For SoilNet, we compare the impact of swapping two different visual segment encoders (PatchCNN vs ResNet-based) and loss functions (embedding-based vs cross-entropy). In partitions C and D the results for these four variants are presented, obtained using the two teacher forcing strategies introduced in subsection 4.5. Between the two strategies, we observe that the linearly decreasing teacher forcing leads to much better results for the horizon symbol prediction metrics across all model configurations. This is likely due to the fact that, in the second teacher strategy, the models are gradually exposed to their own predictions, which helps them to learn to handle noise and uncertainty from their own predictions. The full teacher forcing, on the other hand, can lead to overfitting on the ground-truth inputs and poor generalization in inference. For depth prediction and tabular metrics, the performance differences are less pronounced, as the ground-truth inputs do not affect the models as much at these stages. Partition D shows the SoilNet trained with the winning teacher strategy.

6 Discussion

Our results highlight the importance of architectures specialized for tasks such as soil modeling. Experiments demonstrate that zero-shot inference with standard LLMs (Table 4, partition A) yields poor performance for the complex soil horizon classification task, even on simplified versions of Task 1 and Task 3. Both LLMs evaluated achieve IoU scores below the random guessing baseline (Table 1) and top-1 horizon classification accuracy lower than several SoilNet variants trained on the full set of 99 horizon labels. These findings hint at the limitations of general-purpose LLMs in addressing specialized, complex domain-specific problems such as soil horizon classification.

Moreover, SoilNet outperforms the pipeline of chained individual task solvers (Table 4, partitions B and D) across most tasks; for the regression task of predicting the number of stones and the depth marker segmentation, SoilNet achieves slightly lower but comparable results. This indicates that jointly optimizing all tasks in an end-to-end multitask setting yields higher predictive performance than independently trained modules coupled only at inference time.

Table 4: SoilNet (D) outperforms baseline of zero-shot LLMs (A) and chained task solvers (B) in most tasks. For context, we show the optimal performance for all tasks obtained by models with access to ground truth of respective previous tasks at inference (E), but not include them in comparison. All test set metrics are given in percents (%), except for Stones MSE. SN = SoilNet, DP = Depth Predictor, TP = Tabular Predictor, HP = Horizon Predictor, {PatchCNN, ResNet} = segment encoder, LSTM = horizon embedding/classification module, Emb = embedding loss, CE = cross entropy, Acc. = Accuracy, Agg. Acc. = Aggregated Accuracy over main symbols (see Appendix C for evaluation metrics and more experiment details).

Model name	Depths	Tabular		Horizon Symbol					
	IoU	Stones MSE	Categ. Acc.	Acc.	F1	Acc. @5	Prec. @5	Rec. @5	Agg. Acc.
A. Zero-shot LLM baseline on simplified Task 1 and 3 (5 images, 12 horizon labels, see Appendix A)									
Gemini 2.0 Flash	41.09	-	-	40.0	-	-	-	-	-
ChatGPT-4o mini	36.08	-	-	32.0	-	-	-	-	-
B. Individual task solvers (using predictions of previous tasks)									
Baseline_ResNet_LSTM_Emb	51.74	1.58	46.22	26.40	0.85	33.54	15.44	9.91	45.27
Baseline_ResNet_LSTM_CE	51.74	1.59	46.12	25.34	0.81	47.05	22.46	9.64	41.17
C. SoilNet (Full Teacher Forcing)									
SN_PatchCNN_LSTM_Emb	51.41	8.03	46.82	25.91	1.87	39.97	25.45	15.80	52.35
SN_ResNet_LSTM_Emb	50.90	1.60	45.84	24.84	0.80	33.91	17.07	10.03	42.84
SN_PatchCNN_LSTM_CE	49.53	8.89	47.72	29.85	1.62	56.43	21.34	13.04	53.58
SN_ResNet_LSTM_CE	51.41	1.99	47.39	27.90	1.48	57.61	28.00	15.37	48.60
D. SoilNet (Linearly decreasing Teacher Forcing over 5 Epochs)									
SN_PatchCNN_LSTM_Emb	51.25	8.92	46.60	36.27	7.55	60.21	40.27	33.84	71.42
SN_ResNet_LSTM_Emb	51.47	1.74	47.64	35.40	6.58	59.65	33.75	33.08	68.70
SN_PatchCNN_LSTM_CE	49.52	12.38	46.47	43.99	7.20	72.02	50.33	30.33	68.61
SN_ResNet_LSTM_CE	49.91	1.99	48.08	45.70	7.99	76.25	49.85	35.03	69.88
E. Individual task solvers (using ground truth of previous task for inference, see subsection 5.1)									
DP_MaskedResNet_LSTM	51.74	-	-	-	-	-	-	-	-
TP_ResNet_LSTM	-	1.30	47.59	-	-	-	-	-	-
HP_ResNet_LSTM_Emb	-	-	-	47.75	14.69	72.27	50.56	49.01	78.99
HP_ResNet_LSTM_CE	-	-	-	48.14	11.13	78.88	59.00	44.03	69.41

The individually trained task-specific solvers using ground truth information from the respective previous tasks (Table 4, partition E) establish strong upper bounds for each task. Note that these may not be used for prediction in real applications, since they require ground truth information. SoilNet, without access to that ground truth information, often achieves similar predictive performance. The difference between these upper bounds using ground truth and SoilNet for horizon symbol metrics suggests that performance in the intermediate tasks (depth marker and tabular prediction) has a great impact on the final horizon classification performance.

Within the SoilNet configurations (Table 4, partition D), the variant using the ResNet-based segment encoder generally surpasses the PatchCNN alternative across most evaluation metrics. Regarding training objectives, the best performance in terms of aggregated main symbol accuracy is obtained using the *embedding-based cosine loss*, indicating that semantically structured label representations provide a more effective learning signal than conventional categorical targets. The differences in the aggregated accuracy between the different SoilNet configurations are, however, not as pronounced as in the individual Task 3 solvers.

Beyond the specific use case addressed in this paper, the modular architecture we present - designed for multimodal classification with intra-sample sequential dependencies and a hierarchical label structure - may serve as a generalizable template for related problems in other domains. Similar settings arise in tasks such as: i) *medical imaging*, where multimodal inputs e.g. scans and patient meta-data must be segmented into anatomically meaningful regions with hierarchical diagnoses [12, 20]; ii) *remote sensing*, where satellite imagery (combined multispectral and hyperspectral) is segmented into land cover zones that follow spatial sequences and taxonomies [24]; iii) *document layout analy-*

sis, where textual and visual cues jointly inform the sequential classification of structured document elements [8].

Several simplifications and design choices introduce limitations in our SoilNet pipeline. First, we trained our model on a reduced set of horizon labels. While this was necessary to manage class imbalance, it also limits the model’s ability to generalize to the full complexity of the horizon taxonomy, where label distributions are significantly more skewed. Second, in modeling mixture horizons, we assigned fixed weights of the parent embeddings to each mixture label (see Equation 20 in subsection 4.4). More nuanced strategies, such as learning mixture weights as trainable parameters or defining expert-informed weights per mixture, could better capture the semantic asymmetry and domain-specific knowledge involved in these transitions. Third, despite their semantic grounding, our graph-based label embeddings are outperformed on certain metrics by simpler cross-entropy-trained configurations of SoilNet, suggesting that the added structure does not always translate into performance gains across all tasks.

In future work, we plan to develop an application that integrates the SoilNet pipeline into an accessible interface for use in the field. Such a tool would allow users to capture a soil profile image, automatically retrieve geotemporal metadata and obtain real-time predictions for depth segmentation, morphological features and horizon classification. This would facilitate practical deployment for geologists, agronomists and environmental scientists. Additionally, it would be valuable to conduct a systematic evaluation of human expert performance across all three tasks. Benchmarking SoilNet against domain experts not only offers insight into model reliability or label noise, but may also reveal where automation can assist or complement professional interpretation.

7 Conclusion

In this work, we introduced SoilNet, a modular, multimodal, multitask framework for automated soil horizon classification, designed to mirror the structured reasoning process of human experts. Beyond its technical contributions, our research also seeks to raise awareness for the importance of soil modeling in sustaining healthy ecosystems, agricultural productivity and climate stability. As soil degradation continues to threaten food security and biodiversity, the development of modern, scalable, domain-adapted AI solutions becomes increasingly urgent. Our work demonstrates how advances in Machine Learning, when carefully aligned with domain knowledge, can contribute to efficient soil monitoring and enhance scientific understanding.

Acknowledgments and Disclosure of Funding

We thank the Bundesanstalt für Geowissenschaften und Rohstoffe (BGR) for the financial support of this research and particularly Dr. Einar Eberhardt and Dr. Stefan Broda for their valuable expert advice regarding the complex geological aspects of soil horizon classification. This research was also supported by the German Research Foundation (DFG) - Project number: 528483508 - FIP 12.

References

- [1] Background paper: Desertification in the eu. https://www.eca.europa.eu/en/publications/BP_DESERTIFICATION, accessed: 1.02.2025
- [2] Alayrac, J.B., Donahue, J., Luc, P., Miech, A., Barr, I., Hasson, Y., Lenc, K., Mensch, A., Millican, K., Reynolds, M., Ring, R., Rutherford, E., Cabi, S., Han, T., Gong, Z., Samangooei, S., Monteiro, M., Menick, J., Borgeaud, S., Brock, A., Nematzadeh, A., Sharifzadeh, S., Binkowski, M., Barreira, R., Vinyals, O., Zisserman, A., Simonyan, K.: Flamingo: a visual language model for few-shot learning. ArXiv **abs/2204.14198** (2022)
- [3] Barz, B., Denzler, J.: Hierarchy-based image embeddings for semantic image retrieval. In: 2019 IEEE Winter Conference on Applications of Computer Vision (WACV). IEEE (Jan 2019). <https://doi.org/10.1109/wacv.2019.00073>, <http://dx.doi.org/10.1109/WACV.2019.00073>
- [4] Bertinetto, L., Mueller, R., Tertikas, K., Samangooei, S., Lord, N.A.: Making better mistakes: Leveraging class hierarchies with deep networks (2020), <https://arxiv.org/abs/1912.09393>

- [5] Beucher, A., Rasmussen, C.B., Moeslund, T.B., Greve, M.H.: Interpretation of convolutional neural networks for acid sulfate soil classification. *Frontiers in Environmental Science* **9** (2022). <https://doi.org/10.3389/fenvs.2021.809995>, <https://www.frontiersin.org/journals/environmental-science/articles/10.3389/fenvs.2021.809995>
- [6] Brown, T., Mann, B., Ryder, N., Subbiah, M., Kaplan, J.D., Dhariwal, P., Neelakantan, A., Shyam, P., Sastry, G., Askell, A., Agarwal, S., Herbert-Voss, A., Krueger, G., Henighan, T., Child, R., Ramesh, A., Ziegler, D., Wu, J., Winter, C., Hesse, C., Chen, M., Sigler, E., Litwin, M., Gray, S., Chess, B., Clark, J., Berner, C., McCandlish, S., Radford, A., Sutskever, I., Amodei, D.: Language models are few-shot learners. In: Larochelle, H., Ranzato, M., Hadsell, R., Balcan, M., Lin, H. (eds.) *Advances in Neural Information Processing Systems*. vol. 33, pp. 1877–1901. Curran Associates, Inc. (2020), https://proceedings.neurips.cc/paper_files/paper/2020/file/1457c0d6bfc4967418bfb8ac142f64a-Paper.pdf
- [7] Bundesanstalt für Geowissenschaften und Rohstoffe: Soils: Area and spatial information. https://www.bgr.bund.de/EN/Themen/Boden/Flaechen-Rauminformationen/flaechen-rauminformationen_node.html, accessed: 2025-08-05
- [8] Canhui, X., Yuteng, L., Cao, S., Honghong, Z., Hengyue, B., Yinong, C.: Him: hierarchical multimodal network for document layout analysis. *Applied Intelligence* **53**(20), 24314–24326 (Jul 2023). <https://doi.org/10.1007/s10489-023-04782-3>, <https://doi.org/10.1007/s10489-023-04782-3>
- [9] Chen, C.F., Fan, Q., Panda, R.: Crossvit: Cross-attention multi-scale vision transformer for image classification (2021), <https://arxiv.org/abs/2103.14899>
- [10] Deng, J., Berg, A.C., Li, K., Fei-Fei, L.: What does classifying more than 10,000 image categories tell us? In: Daniilidis, K., Maragos, P., Paragios, N. (eds.) *Computer Vision – ECCV 2010*. pp. 71–84. Springer Berlin Heidelberg, Berlin, Heidelberg (2010)
- [11] Fernandez Astudillo, R., Ballesteros, M., Naseem, T., Blodgett, A., Florian, R.: Transition-based parsing with stack-transformers. In: Cohn, T., He, Y., Liu, Y. (eds.) *Findings of the Association for Computational Linguistics: EMNLP 2020*. pp. 1001–1007. Association for Computational Linguistics, Online (Nov 2020). <https://doi.org/10.18653/v1/2020.findings-emnlp.89>, <https://aclanthology.org/2020.findings-emnlp.89/>
- [12] Gu, R., Zhang, Y., Wang, L., Chen, D., Wang, Y., Ge, R., Jiao, Z., Ye, J., Jia, G., Wang, L.: Mmy-net: a multimodal network exploiting image and patient metadata for simultaneous segmentation and diagnosis. *Multimedia Syst.* **30**(2) (Feb 2024). <https://doi.org/10.1007/s00530-024-01260-9>, <https://doi.org/10.1007/s00530-024-01260-9>
- [13] Gupta, T., Kembhavi, A.: Visual programming: Compositional visual reasoning without training. *ArXiv abs/2211.11559* (2022)
- [14] Gyasi, E.K., Purushotham, S.: Advancements in soil classification: An in-depth analysis of current deep learning techniques and emerging trends. *Air, Soil and Water Research* **16**, 11786221231214069 (2023). <https://doi.org/10.1177/11786221231214069>, <https://doi.org/10.1177/11786221231214069>
- [15] Gyasi, E.K., Purushotham, S.: Advancements in soil classification: An in-depth analysis of current deep learning techniques and emerging trends. *Air, Soil and Water Research* **16**, 11786221231214069 (2023). <https://doi.org/10.1177/11786221231214069>, <https://doi.org/10.1177/11786221231214069>
- [16] Gyasi, E.K., Purushotham, S.: Soil-mobinet: A convolutional neural network model base soil classification to determine soil morphology and its geospatial location. *Sensors* **23**(15) (2023). <https://doi.org/10.3390/s23156709>, <https://www.mdpi.com/1424-8220/23/15/6709>
- [17] Hartemink, A., Zhang, Y., Bockheim, J., Curi, N., Silva, S., Grauer-Gray, J., Lowe, D., Krasilnikov, P.: Chapter three - soil horizon variation: A review. *Advances in Agronomy*, vol. 160, pp. 125–185. Academic Press (2020). <https://doi.org/https://doi.org/10.1016/bs.agron.2019.10.003>, <https://www.sciencedirect.com/science/article/pii/S0065211319301087>
- [18] He, K., Zhang, X., Ren, S., Sun, J.: Deep residual learning for image recognition (2015). <https://doi.org/10.48550/ARXIV.1512.03385>, <https://arxiv.org/abs/1512.03385>
- [19] Hiller, M., Ehinger, K.A., Drummond, T.: Perceiving longer sequences with bi-directional cross-attention transformers (2024), <https://arxiv.org/abs/2402.12138>

- [20] Hinterwimmer, F., Guenther, M., Consalvo, S., Neumann, J., Gersing, A., Woertler, K., von Eisenhart-Rothe, R., Burgkart, R., Rueckert, D.: Impact of metadata in multi-modal classification of bone tumours. *BMC Musculoskeletal Disorders* **25**(1) (Dec 2024). <https://doi.org/10.1186/s12891-024-07934-9>, publisher Copyright: © The Author(s) 2024.
- [21] Hrsg.: K.J. Hartmann; A. Bauriegel; U. Dehner; E. Eberhardt; S. Hesse; D. Kühn; W. Martin; F. Waldmann; AG Boden, B.H. (ed.): *Bodenkundliche Kartieranleitung KA6 in 2 Bänden*. Schweizerbart Science Publishers, Stuttgart, Germany (07 2024), http://www.schweizerbart.de/publications/detail/isbn/9783510968695/Bodenkundliche_Kartieranleitung_KA6_in_2
- [22] Huang, S., Dong, L., Wang, W., Hao, Y., Singhal, S., Ma, S., Lv, T., Cui, L., Mohammed, O.K., Patra, B., Liu, Q., Aggarwal, K., Chi, Z., Bjorck, J., Chaudhary, V., Som, S., Song, X., Wei, F.: Language is not all you need: Aligning perception with language models (2023), <https://arxiv.org/abs/2302.14045>
- [23] Jiang, Z.D., Owens, P.R., Zhang, C.L., Brye, K.R., Weindorf, D.C., Adhikari, K., Sun, Z.X., Sun, F.J., Wang, Q.B.: Towards a dynamic soil survey: Identifying and delineating soil horizons in-situ using deep learning. *Geoderma* **401**, 115341 (2021). <https://doi.org/https://doi.org/10.1016/j.geoderma.2021.115341>, <https://www.sciencedirect.com/science/article/pii/S0016706121004213>
- [24] Jiao, L., Sun, W., Yang, G., Ren, G., Liu, Y.: A hierarchical classification framework of satellite multispectral/hyperspectral images for mapping coastal wetlands. *Remote Sensing* **11**(19) (2019). <https://doi.org/10.3390/rs11192238>, <https://www.mdpi.com/2072-4292/11/19/2238>
- [25] Kirillov, A., Mintun, E., Ravi, N., Mao, H., Rolland, C., Gustafson, L., Xiao, T., Whitehead, S., Berg, A.C., Lo, W.Y., Dollár, P., Girshick, R.: Segment anything (2023), <https://arxiv.org/abs/2304.02643>
- [26] Li, L., Zhou, T., Wang, W., Li, J., Yang, Y.: Deep Hierarchical Semantic Segmentation. pp. 1246–1257 (2022), https://openaccess.thecvf.com/content/CVPR2022/html/Li_Deep_Hierarchical_Semantic_Segmentation_CVPR_2022_paper.html
- [27] Lin, H., Cheng, X., Wu, X., Shen, D.: Cat: Cross attention in vision transformer. In: 2022 IEEE International Conference on Multimedia and Expo (ICME). pp. 1–6 (2022). <https://doi.org/10.1109/ICME52920.2022.9859720>
- [28] Lin, Y., Li, Y., Chen, D., Xu, W., Clark, R., Torr, P.H.: Olympus: A universal task router for computer vision tasks. *arXiv preprint arXiv:2412.09612* (2024)
- [29] Mihaylova, T., Martins, A.F.T.: Scheduled sampling for transformers. In: Alva-Manchego, F., Choi, E., Khashabi, D. (eds.) *Proceedings of the 57th Annual Meeting of the Association for Computational Linguistics: Student Research Workshop*. pp. 351–356. Association for Computational Linguistics, Florence, Italy (Jul 2019). <https://doi.org/10.18653/v1/P19-2049>, <https://aclanthology.org/P19-2049/>
- [30] Nickel, M., Kiela, D.: Poincaré Embeddings for Learning Hierarchical Representations (May 2017). <https://doi.org/10.48550/arXiv.1705.08039>, <http://arxiv.org/abs/1705.08039>, arXiv:1705.08039 [cs]
- [31] de Oliveira, K.M., Falcioni, R., Gonçalves, J.V.F., de Oliveira, C.A., Mendonça, W.A., Crusiol, L.G.T., de Oliveira, R.B., Furlanetto, R.H., Reis, A.S., Nanni, M.R.: Rapid determination of soil horizons and suborders based on vis-nir-swir spectroscopy and machine learning models. *Remote Sensing* **15**(19) (2023). <https://doi.org/10.3390/rs15194859>, <https://www.mdpi.com/2072-4292/15/19/4859>
- [32] Prabhavathi, V., Kuppusamy, P.: A study on deep learning based soil classification. In: 2022 IEEE 4th International Conference on Cybernetics, Cognition and Machine Learning Applications (ICCCMLA). pp. 428–433 (2022). <https://doi.org/10.1109/ICCCMLA56841.2022.9989293>
- [33] Ronaldo, A.: Effective soil type classification using convolutional neural network. *International Journal of Informatics and Computation* **3**, 20 (10 2021). <https://doi.org/10.35842/ijicom.v3i1.33>
- [34] Sak, H., Senior, A., Beaufays, F.: Long short-term memory based recurrent neural network architectures for large vocabulary speech recognition (2014), <https://arxiv.org/abs/1402.1128>

- [35] Schowalter, T.D.: 14 - decomposition and pedogenesis. In: Schowalter, T.D. (ed.) *Insect Ecology* (Second Edition), pp. 405–435. Academic Press, Burlington, second edition edn. (2006). <https://doi.org/https://doi.org/10.1016/B978-012088772-9/50040-6>, <https://www.sciencedirect.com/science/article/pii/B9780120887729500406>
- [36] Sechidis, K., Tsoumakas, G., Vlahavas, I.: On the stratification of multi-label data. In: Gunopulos, D., Hofmann, T., Malerba, D., Vazirgiannis, M. (eds.) *Machine Learning and Knowledge Discovery in Databases*. pp. 145–158. Springer Berlin Heidelberg, Berlin, Heidelberg (2011)
- [37] Shah, A., Zhou, L., Abrámoff, M., Wu, X.: Multiple surface segmentation using convolution neural nets: application to retinal layer segmentation in oct images. *Biomedical Optics Express* **9**, 4509–4526 (08 2018). <https://doi.org/10.1364/BOE.9.004509>
- [38] Shen, Y., Song, K., Tan, X., Li, D., Lu, W., Zhuang, Y.: Hugginggpt: Solving ai tasks with chatgpt and its friends in huggingface. In: *Advances in Neural Information Processing Systems* (2023)
- [39] Spaargaren, O.C., Deckers, J.: The world reference base for soil resources. In: Schulte, A., Ruyiat, D. (eds.) *Soils of Tropical Forest Ecosystems*. pp. 21–28. Springer Berlin Heidelberg, Berlin, Heidelberg (1998)
- [40] Surís, D., Menon, S., Vondrick, C.: Vipergpt: Visual inference via python execution for reasoning (2023), <https://arxiv.org/abs/2303.08128>
- [41] Teixeira, I., Morais, R., Sousa, J.J., Cunha, A.: Deep learning models for the classification of crops in aerial imagery: A review. *Agriculture* **13**(5) (2023). <https://doi.org/10.3390/agriculture13050965>, <https://www.mdpi.com/2077-0472/13/5/965>
- [42] Thünen Institute: German Agricultural Soil Inventory (BZE-LW). <https://www.thuenen.de/en/institutes/climate-smart-agriculture/projects/agricultural-soil-inventory-bze-lw>, accessed: 2025-08-05
- [43] Turk, J.: jellyfish (Jun 2023), <https://github.com/jamesturk/jellyfish>
- [44] Yamagata, T., Ikeno, H., Kimura, T., Isokawa, T., Nakaji, T., Mori, K., Kume, T., Ohashi, M.: Segmenting growing and dying woody roots in a forest using deep learning-based software. In: *TENCON 2024 - 2024 IEEE Region 10 Conference (TENCON)*. pp. 535–538 (2024). <https://doi.org/10.1109/TENCON61640.2024.10902758>
- [45] Yan, Z., Zhang, H., Piramuthu, R., Jagadeesh, V., DeCoste, D., Di, W., Yu, Y.: Hd-cnn: Hierarchical deep convolutional neural network for large scale visual recognition (2015), <https://arxiv.org/abs/1410.0736>
- [46] Zhu, X., Bain, M.: B-cnn: Branch convolutional neural network for hierarchical classification (2017), <https://arxiv.org/abs/1709.09890>

A Horizon Segmentation and Classification with LLMs

We tested the zero-shot performance of two standard LLMs on simplified versions of Tasks 1 and 3: Gemini 2.0 Flash (<https://gemini.google.com/app/>) and ChatGPT-4o mini (<https://chat.openai.com/chat>), both accessed between 5.-11.05.2025. Our approach was as follows:

- 1) We first explained the tasks to the LLM.
- 2) We uploaded in the chat five random soil profile images from our training set along with their ground truth lists of depth markers and corresponding horizon labels. Here, we prompted the LLM to analyze the images with the accompanying target information and update its memory accordingly. In total, the five training images contained 12 different horizon labels.
- 3) We uploaded 5 new images from our validation set and asked the LLM to predict the depths and horizon labels on its own. We selected the five images also randomly, but took care that they only contain horizon labels that the LLM has already seen in the previous five examples.
- 4) We computed the 1D-IoU and top-1 horizon accuracy for the LLMs' predictions.

The results are displayed together with the SoilNet results in Table 4. The chat histories are publicly available at:

- <https://g.co/gemini/share/0ad1d2bf5561>
- <https://chatgpt.com/share/681f47c2-8484-800d-bdc4-ec5c10e72b4e>

B Computing the Horizon Embeddings

This section presents and proves the similarity guarantees offered by the horizon embeddings and walks the reader through a simple numerical example with 10 horizon embeddings.

B.1 Similarity Invariances

Depending on the order in which they are computed, the label embeddings may land in different subspaces within the embedding space \mathbb{R}^{d_E} . However, the algorithm guarantees invariant inner products between all categories of label combinations. Without loss of generality, let the equation of a (normalized) mixture embedding be written as:

$$\varphi(h_3) = \frac{\frac{1}{3}\varphi(h_1) + \frac{2}{3}\varphi(h_2)}{\|\frac{1}{3}\varphi(h_1) + \frac{2}{3}\varphi(h_2)\|} = \frac{1}{\sqrt{5}}(\varphi(h_1) + 2\varphi(h_2)) \quad (21)$$

since $\|\varphi(h_1)\| = \|\varphi(h_2)\| = 1$ and $\varphi(h_1) \perp \varphi(h_2)$. The embeddings of the mixture parents will always be orthogonal on each other because a mixture is always composed of labels containing different main symbols.

Then, the following inner product identities hold⁶:

- 1) By definition, the dot product of any two labels (mixtures or non-mixtures) that do not have any main symbol in common is 0. Example: **Ah** vs **Bt**, **Ah-Bv** vs **Sd** or **Ah-Bv** vs **M-Sw**.
- 2) Two non-mixture labels belonging to the same main symbol will always have similarity $\frac{1}{2}$ - see Equation 16 and Equation 17. Example: **Al** vs **Ah**.
- 3) Mixture vs Non-mixture:
 - 3.1) The non-mixture is one of the parents in the mixture: the dot product is $\frac{1}{\sqrt{5}}$, if the non-mixture label is identical to the first parent in the mixture e.g. **Al** vs **Al-Bt**, and $\frac{2}{\sqrt{5}}$, if the non-mixture is identical to the second (dominant) parent in the mixture e.g. **Bt** vs **Al-Bt**.

⁶For conciseness and readability, we will henceforth denote the dot product (or similarity) of the embeddings of two horizon labels simply as the dot product of those labels, while asking the reader to keep in mind that labels are strings and embeddings are vectors.

Proof. Let $\varphi(h_3)$ be defined as in Equation 21. Then:

$$\begin{aligned}\langle \varphi(h_1), \varphi(h_3) \rangle &= \frac{1}{\sqrt{5}} \langle \varphi(h_1), \varphi(h_1) + 2 \cdot \varphi(h_2) \rangle \\ &= \frac{1}{\sqrt{5}} (\underbrace{\langle \varphi(h_1), \varphi(h_1) \rangle}_1 + 2 \cdot \underbrace{\langle \varphi(h_1), \varphi(h_2) \rangle}_0) = \frac{1}{\sqrt{5}}\end{aligned}$$

Analogously:

$$\begin{aligned}\langle \varphi(h_2), \varphi(h_3) \rangle &= \frac{1}{\sqrt{5}} \langle \varphi(h_2), \varphi(h_1) + 2 \cdot \varphi(h_2) \rangle \\ &= \frac{1}{\sqrt{5}} (\underbrace{\langle \varphi(h_2), \varphi(h_1) \rangle}_0 + 2 \cdot \underbrace{\langle \varphi(h_2), \varphi(h_2) \rangle}_1) = \frac{2}{\sqrt{5}}\end{aligned}$$

□

- 3.2) The non-mixture is not one of the parents in the mixture, but has a common main symbol with one of the parents: the dot product is $\frac{1}{2\sqrt{5}}$, if the common main symbol comes from the first parent e.g. **Ah** vs **Al-Bt**, and $\frac{1}{\sqrt{5}}$ otherwise, e.g. **Bv** vs **Al-Bt**.

Proof. Let $\varphi(h_3)$ be defined as in Equation 21. Then:

$$\begin{aligned}\langle \varphi(h_1), \varphi(h_3) \rangle &= \frac{1}{\sqrt{5}} \langle \varphi(h_1), \varphi(h_1) + 2 \cdot \varphi(h_2) \rangle \\ &= \frac{1}{\sqrt{5}} (\underbrace{\langle \varphi(h_1), \varphi(h_1) \rangle}_{1/2} + 2 \cdot \underbrace{\langle \varphi(h_1), \varphi(h_2) \rangle}_0) = \frac{1}{2\sqrt{5}}\end{aligned}$$

Analogously:

$$\begin{aligned}\langle \varphi(h_2), \varphi(h_3) \rangle &= \frac{1}{\sqrt{5}} \langle \varphi(h_2), \varphi(h_1) + 2 \cdot \varphi(h_2) \rangle \\ &= \frac{1}{\sqrt{5}} (\underbrace{\langle \varphi(h_2), \varphi(h_1) \rangle}_0 + 2 \cdot \underbrace{\langle \varphi(h_2), \varphi(h_2) \rangle}_{1/2}) = \frac{1}{\sqrt{5}}\end{aligned}$$

□

4) Mixture vs Mixture:

- 4.1) The mixtures have one parent in common. Through analogous steps as the ones above, one arrives at the following results:
- 4.1.1) If the common parent is at the second position e.g. **Ah-Bv** vs **Sd-Bv**, the dot product is $\frac{4}{5}$.
 - 4.1.2) If the common parent is at the first position e.g. **Bv-Cv** vs **Bv-Ael**, the dot product is $\frac{1}{5}$.
 - 4.1.3) If the common parent is at the first position in one mixture and second position in the other mixture e.g. **Ah-Bv** vs **Bv-Cv**, the dot product is $\frac{2}{5}$.
- 4.2) The mixtures have no common parent, but one common main symbol. Through analogous steps as the ones above, one arrives at the following results:
- 4.2.1) One common main symbol at the first positions, different main symbols at the second positions e.g. **Sd-Bv** vs **Sw-Ah**: the dot product is $\frac{1}{10}$.
 - 4.2.2) Two common main symbols at the same positions e.g. **Ah-Bv** vs **Al-Bt**: the dot product is $\frac{1}{2}$ (consistent with property 2) above, built in the algorithm itself).
 - 4.2.3) One common main symbol at crossed positions, the remaining positions have different main symbols e.g. **Ah-Bv** vs **Sw-Ap**: the dot product is $\frac{1}{5}$.
 - 4.2.4) Two common main symbols at crossed positions e.g. **Ah-Bv** vs **Bt-Al**: the dot product is $\frac{2}{5}$.
 - 4.2.5) One common main symbol at the second position, different main symbols at the first position e.g. **Ah-Bv** vs **Sd-Bt**: the dot product is $\frac{2}{5}$.

B.2 Numerical Example

Following is an example of how the graph embeddings are computed in a simplified setting with horizons from only four main classes: two classes with single representatives ($h_1 = \mathbf{iC}$ and $h_2 = \mathbf{Gor}$), two classes with multiple representatives ($h_3 = \mathbf{Al}$, $h_4 = \mathbf{Ael}$, $h_5 = \mathbf{Acp}$ and $h_6 = \mathbf{Bt}$, $h_7 =$

\mathbf{Bs} , $h_8 = \mathbf{Bv}$, $h_9 = \mathbf{Btv}$) that also have a mixture $h_{10} = \mathbf{Al-Bv}$. This means that the embedding space dimension here is $d_E = 9$, with $\varphi(h_i) \in \mathbb{R}^9, \forall i = 1, \dots, 10, N = 10$ (recall that mixtures do not add dimensionality to this space). $e_i \in \mathbb{R}^9$ denotes the unity vector with 1 at the i -th coordinate and 0's everywhere else.

1. $\varphi(h_1) = e_1$ (**iC**)

2. $\varphi(h_2) = e_2$ (**Gor**)

3. $\varphi(h_3) = e_3$ (**Al**)

$$3.1. \left. \begin{aligned} \varphi(h_4)^T \cdot \varphi(h_1) &\stackrel{!}{=} s(h_4, h_1) = 1 - 1 = 0 \\ \varphi(h_4)^T \cdot \varphi(h_2) &\stackrel{!}{=} s(h_4, h_2) = 1 - 1 = 0 \\ \varphi(h_4)^T \cdot \varphi(h_3) &\stackrel{!}{=} s(h_4, h_3) = 1 - \frac{1}{2} = \frac{1}{2} \end{aligned} \right\} \iff \left\{ \begin{aligned} \varphi(h_4)_1 \cdot 1 &= 0 \\ \varphi(h_4)_2 \cdot 1 &= 0 \\ \varphi(h_4)_3 \cdot 1 &= \frac{1}{2} \end{aligned} \right\} \implies$$

$$\implies \hat{\varphi}(h_4) = \left(0, 0, \frac{1}{2}\right)^T$$

$$\implies \varphi(h_4)_4 = \sqrt{1 - \|\hat{\varphi}(h_4)\|^2} = \sqrt{1 - \frac{1}{4}} = \frac{\sqrt{3}}{2}$$

$$\implies \varphi(h_4) = \left(0, 0, \frac{1}{2}, \frac{\sqrt{3}}{2}, 0, \dots, 0\right)^T \text{ (**Ael**)}$$

$$3.2. \left. \begin{aligned} \varphi(h_5)^T \cdot \varphi(h_1) &\stackrel{!}{=} s(h_5, h_1) = 1 - 1 = 0 \\ \varphi(h_5)^T \cdot \varphi(h_2) &\stackrel{!}{=} s(h_5, h_2) = 1 - 1 = 0 \\ \varphi(h_5)^T \cdot \varphi(h_3) &\stackrel{!}{=} s(h_5, h_3) = 1 - \frac{1}{2} = \frac{1}{2} \\ \varphi(h_5)^T \cdot \varphi(h_4) &\stackrel{!}{=} s(h_5, h_4) = 1 - \frac{1}{2} = \frac{1}{2} \end{aligned} \right\} \iff$$

$$\iff \left\{ \begin{aligned} \varphi(h_5)_1 \cdot 1 &= 0 \\ \varphi(h_5)_2 \cdot 1 &= 0 \\ \varphi(h_5)_3 \cdot 1 &= \frac{1}{2} \\ \varphi(h_5)_3 \cdot \varphi(h_4)_3 + \varphi(h_5)_4 \cdot \varphi(h_4)_4 &= \frac{1}{2} \cdot \frac{1}{2} + \varphi(h_5)_4 \cdot \frac{\sqrt{3}}{2} = \frac{1}{2} \end{aligned} \right\} \implies$$

$$\implies \hat{\varphi}(h_5) = \left(0, 0, \frac{1}{2}, \frac{\sqrt{3}}{6}\right)^T$$

$$\implies \varphi(h_5)_5 = \sqrt{1 - \|\hat{\varphi}(h_5)\|^2} = \sqrt{1 - \left(\frac{1}{4} + \frac{1}{12}\right)} = \sqrt{1 - \frac{1}{3}} = \frac{\sqrt{6}}{3}$$

$$\implies \varphi(h_5) = \left(0, 0, \frac{1}{2}, \frac{\sqrt{3}}{6}, \frac{\sqrt{6}}{3}, 0, \dots, 0\right)^T \text{ (**Acp**)}$$

4. $\varphi(h_6) = e_6$ (**Bt**)

4.1. $\varphi(h_7) = \left(0, \dots, 0, \frac{1}{2}, \frac{\sqrt{3}}{2}, 0, 0\right)^T$ (**Bs**, analogous to 3.1)

4.2. $\varphi(h_8) = \left(0, \dots, 0, \frac{1}{2}, \frac{\sqrt{3}}{6}, \frac{\sqrt{6}}{3}, 0\right)^T$ (**Bv**, analogous to 3.2)

4.3. Leaving out the dot products equaling 0 here:

$$\left. \begin{aligned} \varphi(h_9)^T \cdot \varphi(h_6) &\stackrel{!}{=} s(h_9, h_6) = \frac{1}{2} \\ \varphi(h_9)^T \cdot \varphi(h_7) &\stackrel{!}{=} s(h_9, h_7) = \frac{1}{2} \\ \varphi(h_9)^T \cdot \varphi(h_8) &\stackrel{!}{=} s(h_9, h_8) = \frac{1}{2} \end{aligned} \right\} \iff$$

$$\begin{aligned}
&\Leftrightarrow \left\{ \begin{array}{l} \varphi(h_9)_6 \cdot \varphi(h_6)_6 = \frac{1}{2} \\ \varphi(h_9)_6 \cdot \varphi(h_7)_6 + \varphi(h_9)_7 \cdot \varphi(h_7)_7 = \frac{1}{2} \\ \varphi(h_9)_6 \cdot \varphi(h_8)_6 + \varphi(h_9)_7 \cdot \varphi(h_8)_7 + \varphi(h_9)_8 \cdot \varphi(h_8)_8 = \frac{1}{2} \end{array} \right\} \Rightarrow \\
&\Rightarrow \left\{ \begin{array}{l} \varphi(h_9)_6 \cdot 1 = \frac{1}{2} \Rightarrow \varphi(h_9)_6 = \frac{1}{2} \\ \frac{1}{2} \cdot \frac{1}{2} + \varphi(h_9)_7 \cdot \frac{\sqrt{3}}{2} = \frac{1}{2} \Rightarrow \varphi(h_9)_7 = \frac{\sqrt{3}}{6} \\ \frac{1}{2} \cdot \frac{1}{2} + \frac{\sqrt{3}}{6} \cdot \frac{\sqrt{3}}{6} + \varphi(h_9)_8 \cdot \frac{\sqrt{6}}{3} = \frac{1}{2} \Rightarrow \varphi(h_9)_8 = \frac{\sqrt{6}}{12} \end{array} \right\} \Rightarrow \\
&\Rightarrow \hat{\varphi}(h_9) = \left(0, \dots, 0, \frac{1}{2}, \frac{\sqrt{3}}{6}, \frac{\sqrt{6}}{12} \right)^T \in \mathbb{R}^8 \\
&\Rightarrow \varphi(h_9)_9 = \sqrt{1 - \|\hat{\varphi}(h_9)\|^2} = \sqrt{1 - \left(\frac{1}{4} + \frac{1}{12} + \frac{1}{24} \right)} = \sqrt{1 - \frac{3}{8}} = \frac{\sqrt{10}}{4} \\
&\Rightarrow \varphi(h_5) = \left(0, \dots, 0, \frac{1}{2}, \frac{\sqrt{3}}{6}, \frac{\sqrt{6}}{12}, \frac{\sqrt{10}}{4} \right)^T \quad (\mathbf{Btv})
\end{aligned}$$

$$5. \varphi(h_{10}) = \frac{1}{3}\varphi(h_3) + \frac{2}{3}\varphi(h_8) \quad (\mathbf{Al-Bv})$$

$$\text{Set } \varphi(h_{10}) \leftarrow \varphi(h_{10}) / \|\varphi(h_{10})\|$$

C Compute Resources, Hyperparameters and Evaluation Metrics

In this section, we provide additional details on the computational resources and hyperparameters used in our experiments.

Experiment Compute Settings. The experiments were conducted on our internal compute cluster, shared with other researchers. We used NVIDIA B200 GPUs with a total of 180GB of VRAM each. Each experiment was run on a single GPU, without any distributed training or data parallelism. The training was done using the PyTorch framework (PyTorch 2.7.0 with CUDA 12.8) and the experiment results were tracked on Weights & Biases (<https://wandb.ai/site>). For the end-to-end SoilNet models, the training took on average 45 minutes per experiment and an average memory usage of 150GB of VRAM on the GPU. We report 8 experiments for the end-to-end SoilNet models, which makes a total of 6 hours of training time. For the individual tasks the memory usage as well as the training time was lower, with an average of 25 minutes per experiment and an average memory usage of 100GB of VRAM on the GPU. We report 8 experiments for the individual tasks, which makes a total of 2.5 hours of training time. With the unreported experiments neglected, the total training time for all experiments is 8.5 hours.

Hyperparameters. In our experiments, we used common default hyperparameters with minimal adjustments from preliminary trials, without performing extensive searches. Table 5 shows the hyperparameters used for all experiments in this paper. For the additional hyperparameters specific to each experiment and model configuration, the readers may consult our code repository, where we list them at the end of the experiment files.

Table 5: Hyperparameters used for all experiments.

Hyperparameter	Value
Batch size	8
Number of workers	16
Optimizer	AdamW
Learning rate	0.0001
Dropout	0.1
Weight decay	0.01
Maximum epochs	100
Early stopping patience	5

We emphasize several metrics we used to evaluate performance on the three tasks:

1D-IoU. We wrote a simplified form of the standard Intersection over Union (IoU) used for evaluating object detection models. Our 1D-IoU metric is designed to evaluate the alignment between predicted and ground truth depth markers. It computes the overlap-to-union ratio for corresponding horizontal horizon stripes, assigning a zero intersection to the disjoint intervals.

Precision@k and Recall@k. For the classification tasks, we compute precision@k and recall@k macro-averaged across all classes, which account for the top-k predicted labels for each sample, providing a more nuanced assessment of the model’s ability to rank relevant labels effectively.

Aggregated Accuracy over Main Symbols. To better understand the nature of misclassifications made by the model, we compute the accuracy over the 10 main horizon symbols that constitute the first layer of the hierarchical label graph. This aggregation allows us to distinguish between minor label deviations, where the predicted label still falls into the correct main symbol, and complete structural misclassifications, where the prediction misses the correct main symbol. In the case of mixture horizons, the second label is counted for the predicted main symbol (see Equation 20).

D Full Metrics Tables for Individual Tabular Prediction

In section 5.1, Table 2 shows the aggregated metrics for the categorical features for the two configurations of the individual tabular predictor (Task 2). Here in Table 6, we present the full metrics tables for predicting the morphological horizon-specific features. Both configurations use LSTM as tabular prediction modules for the six tabular horizon features. They differ in the segment encoder: one uses the custom PatchCNN and the other the ResNet-based segment encoder (see subsection 4.2). The ResNet-based tabular predictor outperforms the PatchCNN counterpart.

Table 6: Full tables for individual tabular prediction metrics (Task 2). Metrics on the test set. TP = Tabular Predictor, {PatchCNN, ResNet} = segment encoder, LSTM = tabular prediction module, Acc. = Accuracy, Prec. = Precision, Rec. = Recall.

TP_PatchCNN_LSTM								
Feature	MSE	Acc. (%)	F1 (%)	Prec. (%)	Rec. (%)	Acc.@3 (%)	Prec.@3 (%)	Rec.@3 (%)
Stones	6.11	-	-	-	-	-	-	-
Soil Type	-	34.55	17.02	25.72	17.25	65.56	52.08	36.96
Soil Color	-	24.15	2.38	4.55	3.49	49.98	19.48	10.11
Carbonate	-	72.57	21.03	39.79	22.88	92.06	74.37	52.84
Humus	-	54.57	32.97	34.75	33.00	91.20	87.64	67.14
Rooting	-	36.79	27.70	32.56	30.33	74.54	74.81	70.55

TP_ResNet_LSTM								
Feature	MSE	Acc. (%)	F1 (%)	Prec. (%)	Rec. (%)	Acc.@3 (%)	Prec.@3 (%)	Rec.@3 (%)
Stones	1.30	-	-	-	-	-	-	-
Soil Type	-	34.99	20.20	25.81	21.23	69.35	67.62	48.77
Soil Color	-	29.37	5.53	6.77	5.75	57.74	20.08	14.18
Carbonate	-	78.38	20.29	31.06	21.43	92.73	81.68	49.58
Humus	-	56.16	40.82	42.39	45.26	92.66	88.82	84.61
Rooting	-	39.04	33.93	41.19	33.92	77.14	81.87	73.55

E Confusion Matrices for Individual Horizon Classification

We show here only the confusion matrices aggregated on the main symbol level for two individual Task 3 solvers (Figure 7). The full confusion matrices for these two examples with all 99 horizon symbols can be found in our repository, as well as matrices for other horizon predictors.

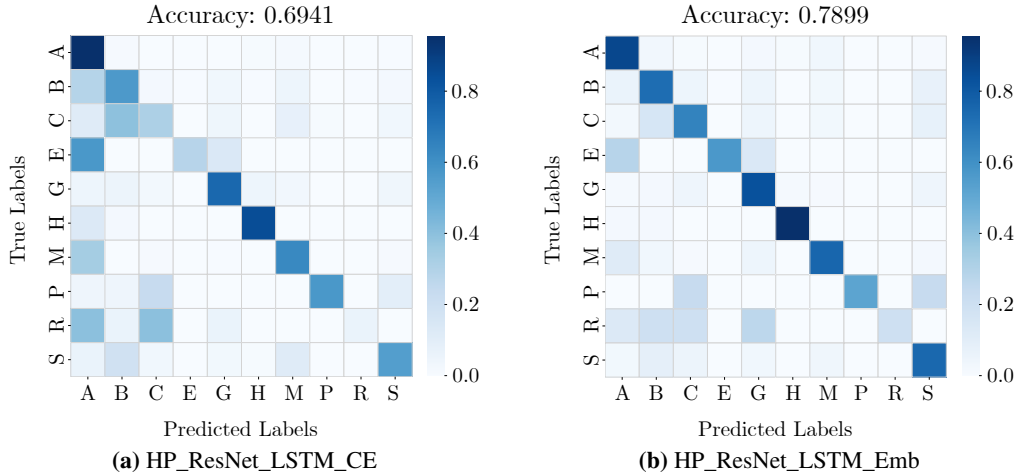


Figure 7: An embedding-based horizon classifier predicts the main symbol more accurately than a classifier trained on one-hot encodings. The confusion matrices are aggregated on the main symbol hierarchy.

HP = Horizon Predictor, ResNet = segment encoder (see subsection 4.2), LSTM = horizon classification module, Emb = embedding loss, CE = cross entropy.